

## An integrated configuration with robust interfacial contact for durable and flexible zinc ion batteries



Penghui Chen <sup>a,b</sup>, Weiya Zhou <sup>a,b,c,d,\*</sup>, Zhuojian Xiao <sup>a,b</sup>, Shaoqing Li <sup>a,b</sup>, Zibo Wang <sup>a,b</sup>, Yanchun Wang <sup>a,c</sup>, Sishen Xie <sup>a,b,c,d,\*\*</sup>

<sup>a</sup> Beijing National Laboratory for Condensed Matter Physics, Institute of Physics, Chinese Academy of Sciences, Beijing, 100190, China

<sup>b</sup> University of Chinese Academy of Sciences, Beijing, 100049, China

<sup>c</sup> Beijing Key Laboratory for Advanced Functional Materials and Structure Research, Beijing, 100190, China

<sup>d</sup> Songshan Lake Materials Laboratory, Dongguan, Guangdong, 523808, China

### ARTICLE INFO

#### Keywords:

Integrated configuration  
Dendrite-free anode  
Durability  
Interfacial contact  
Flexible zinc ion battery

### ABSTRACT

The flexible zinc ion battery (ZIB) is deemed to be a promising candidate for flexible power supply due to its high security and low cost. However, conventional segregated battery configuration inevitably suffers from the relative displacement or detachment between two neighboring components at bending strain, which seriously degrade the performance of a flexible battery. Moreover, stubborn Zn dendrite drastically shortens the cycle life. Herein, by integrating Zn anode, zinc protective coating, polyamide separator and cathode into a single matrix, referred as the integrated electrode, a long cycle life and robust flexibility for ZIB in aqueous electrolyte are achieved. Seamless connection with the adjacent layers not only avoids the relative displacement or detachment caused by bending strain, but enhances the interfacial contact to promote the electrochemical kinetics. The built-in protective coating in the integrated configuration significantly inhibits the dendrites and side reactions for extending the durability. Furthermore, the integrated configuration makes the whole battery lighter, thinner and more powerful. Therefore, this work provides a new design idea for engineering innovative battery configuration and enables high performances for a flexible ZIB. Meanwhile, the research results would deliver great potential applications in flexible electronics and boost the development of configuration of energy storage devices.

### 1. Introduction

The boom in wearable electronics has triggered brisk demands for nonflammable, reliable, cost-efficient and flexible electrochemical energy storage devices with superior performances [1–5]. In virtue of the inherent safety, cost effectiveness and facile assemble process, the aqueous rechargeable zinc ion battery (ZIB) is a promising candidate among various energy storage devices [6–8]. Spontaneously, ZIBs with good flexibility are urgently needed. Traditionally, like lithium ion batteries, ZIBs are constructed by sandwiching a separator into two electrodes. However, in the conventional configuration, since separator is situated separately between two isolated electrodes, the different curvature radii of different components create a considerable displacement or detachment between them under bending states, which induces a surge of contact resistances and relevant deterioration of electrochemical performances [9,10]. This situation will be further

deteriorated especially in an aqueous environment. Therefore, solid or quasi-solid electrolytes with excellent mechanical properties are introduced to promote the mechanical and electrochemical properties of flexible batteries [11–13]. Unfortunately, unlike aqueous electrolytes that have good wettability with electrodes, the rigid contacts between the nonliquid electrolytes and electrodes result in larger interfacial resistances [14,15]. Moreover, the currently used nonliquid electrolytes are fabricated by simply mixing chemically inert organic materials and liquid solutions, which is detrimental to ionic conductivity [16]. Hence, on the basis of keeping the advantages of high ionic conductivity and good infiltration of aqueous electrolyte, it is deserved to develop an unique structure for flexible ZIB so that all components still possess robust interfacial contact even at the bending states.

Integrated configuration, in which all components are incorporated into one, has delivered new insights into the rational regulation of various flexible energy storage devices. Typically, all components

\* Corresponding author. Beijing National Laboratory for Condensed Matter Physics, Institute of Physics, Chinese Academy of Sciences, Beijing, 100190, China.

\*\* Corresponding author. Beijing National Laboratory for Condensed Matter Physics, Institute of Physics, Chinese Academy of Sciences, Beijing, 100190, China.

E-mail addresses: [wyzhou@iphy.ac.cn](mailto:wyzhou@iphy.ac.cn) (W. Zhou), [ssxie@iphy.ac.cn](mailto:ssxie@iphy.ac.cn) (S. Xie).

including electrodes, separator, and even current collectors are assembled together in an integral whole, leading to a continuously seamless connection between the neighboring components. Benefiting from this configuration, flexible devices can not only achieve enhanced interfacial contact between the adjacent components but also ensure steady transportation efficiency of ions and electrons even though under different bending states [17]. Supercapacitors have earlier carried out the designs of integrated configuration [18–20]. For instance, an epidermal supercapacitor with merely 1  $\mu\text{m}$  thickness has been fabricated based on the integrated configuration, which achieves superior specific capacitance and outstanding flexibility (10<sup>5</sup> times bending) [20]. Besides, recent progresses have been made on the integrated architecture design of various battery systems [21–24]. Nonetheless, the strict requirements for complicated processing and equipments as well as the high-cost materials not only make them difficult to be compatible with current battery manufacturing processes, but also increase the difficulty of scalable production. Enlightened by above approaches, exploiting an ingenious, low-cost and effective way to fabricate high-performance flexible ZIBs with rational integrated configuration is quite fascinating.

Actually, except for the above inadequacy about battery configuration that restricts flexible ZIBs, an intrinsic intractable barrier that entire ZIBs face concerns the notorious dendrite growth of Zn metal anode as well as the consequent poor cycle life-span. Dendrite is a pertinacious problem of various metal anodes such as Li and Zn anodes. More unfortunately, zinc is thermally unstable in aqueous electrolytes even though the electrolyte is neutral or mildly acidic [25]. Consequently, zinc is susceptible to corrosion reactions including hydrogen evolution reaction and oxygen-induced passivation [26,27]. In turn, the resulting local pH change gives detrimental Zn<sup>2+</sup>-insulating by-products (such as Zn hydroxides and zincates) that passivate and break the fresh Zn. A lot of techniques have been developed to tackle the problems mentioned above [26–28]. Quite recently, Cui and his co-workers have developed a protective interphase consist of cost-effective polyamide (PA) and zinc trifluoromethanesulfonate ( $\text{Zn}(\text{TfO})_2$ ) and proved its significant effects on inhibiting zinc dendrites and side reactions [29]. The above protective interphase greatly boosts the cycle stability of ZIBs, however, the routine segregated battery configuration with mediocre interfacial contact restricts the high-rate capability and mechanical flexibility. Additionally, like most ZIBs in the above work, the metal current collector is used to mechanically hold the electrode material and conduct electricity. It is noted that there would be two primary problems using metal current collectors in ZIBs. Firstly, metal current collectors have no contribution to the overall capacity, and the effective mass proportion of active materials in the entire electrode will be vastly brought down, which substantially lowers the specific capacity and energy density of the entire batteries. Secondly, the weak adhesion and limited contact area between current collectors and electrode materials cause gaps associated with volumetric changes of active materials at the material/current collector interface [30]. This gives rise to the capacity loss or poor performance at high rates. And this problem will become more serious in flexible batteries, where desquamations of active materials from current collectors are very likely to take place upon bending. Given all this, how to implant a protective layer into the integrated configuration and get rid of the metal collector while still keep the stability of the active materials must be challenging but absolutely promising.

In this work, we propose an ingenious “all integrated into one” design to engineer a ZIB with integrated configuration for the stable and flexible energy storage. In this elaborate configuration, the PA micro-porous filter membrane, a separator with excellent flexibility and good toughness usually adopted in ZIBs, is attached compactly onto one side of a Zn-metal anode. A built-in  $\text{Zn}(\text{TfO})_2$ -PA protective coating is sandwiched between the Zn anode and PA separator, functioning as a “glue” to bond the Zn anode and PA separator. The cathode composed of  $\alpha\text{-MnO}_2$  nanowires (NWs) and multi-walled carbon nanotubes (MWCNTs) are loaded onto the separator through a common blade

coating method and the entire cathode layer itself functions as its own current collector. In the resulting integrated configuration, there is a strong interaction between the neighboring components to ensure robust interfacial contact. Compared with the conventional loose stacked construction, such an “all integrated into one configuration” can not only create dendrite-free and stable Zn anode to extend the cycle life, but also enhance the interface contact to decreases the polarization of the battery with better rate capability. Meanwhile, the integrated configuration brings the feasibility of cathode part itself replacing the metal current collector and achieves the lightening and thinning of battery. Moreover, robust interfacial adhesion between adjacent components can eliminate relative displacement or detachment under bending states, which holds the favorable flexibility and high strength that are required for flexible electronics. The technique presented here is convenient and scalable combined with its low-cost materials, which provides a promising approach to promote flexible ZIBs.

## 2. Experimental section

### 2.1. Preparation of integrated electrodes

Firstly, 1.0 g PA microfiltration membrane (Shanghai Xingya Purification Materials Factory, pore diameter: 0.22  $\mu\text{m}$ ) was dissolved in 2.0 mL anhydrous formic acid (HCOOH), and then 1.0 g  $\text{Zn}(\text{TfO})_2$  was added to the above solution under continuous stirring until a homogeneous milky white solution was obtained. The fresh Zn foil was cleaned with acetone under ultrasonication and dried in the oven. An appropriate amount of the above mixed solution was then cast onto the Zn foil through the doctor blading method (named as  $\text{Zn}(\text{TfO})_2$ -PA@Zn), and after a few seconds, a piece of tailored enhanced PA microfiltration membrane (Tianjin Jinteng Experimental Equipment Co., Ltd., pore diameter: 0.22  $\mu\text{m}$ ) was attached onto the undried mixed solution. The as-prepared product was rapidly transferred into an oven and dried at 60 °C overnight (The obtained product is named as Integrated Separator@Zn). The cathode slurry was obtained by dispersing 70 mg  $\alpha\text{-MnO}_2$  NWs (prepared by a hydrothermal method as reported previously [31]), 20 mg MWCNTs (10–20 nm in outer diameter and 0.5–2  $\mu\text{m}$  in length, Chengdu Institute of Organic Chemistry, Chinese Academy of Sciences) and 10 mg polyvinylidene fluoride (PVDF) powder in *N*-methyl-2-pyrrolidone (NMP) and stirring for 24 h. Afterwards, the slurry was poured onto another side of the Integrated Separator by the doctor blading method. Then an electrode with integrated configuration was obtained after vacuum drying at 60 °C for 24 h (named as Integrated Electrode). For comparison, the conventional segregated electrode was fabricated by sandwiching the pristine PA separator between the isolated working electrode and Zn foil (named as Segregated Electrode). Working electrode was prepared by coating the same cathode slurry onto a stainless steel (SS) foil and dried at 60 °C for 24 h in a vacuum oven. The mass loadings of above two electrodes were around 1 mg  $\text{cm}^{-2}$ .

### 2.2. Assembly of coin-type and flexible ZIBs

Basic electrochemical properties were measured using CR2025 coin-type cells. The large area Integrated Electrode and Segregated Electrode were cut into disks with a diameter 16 mm to fabricate the coin-cells. Flexible batteries for testing various electrochemical properties were assembled by sealing the integrated electrode and segregated electrode into Al/plastic packages with Zn and stainless steel strips as anode tabs and cathode tabs, respectively. For the integrated batteries, the integrated electrode was immersed into the electrolyte for 1 h before assembly.

### 2.3. Characterizations

The phase purity and crystal structure were identified by X-ray

diffraction (XRD, Bruker, D8 Advance) using a diffractometer with Cu $\kappa$  radiation in the 20 angular range of 10°–80° at a scanning rate of 0.02° s $^{-1}$ . The morphologies and microstructures of the materials and electrodes were observed using field-emission scanning electron microscopy (SEM, Hitachi, S5200) coupled with an energy dispersive X-ray spectroscopy (EDX, Oxford Instrument) spectrometer. The optical surface profilometry was tested using a vertical scanning white-light interfering profilometer (Bruker, Contour GT). The tensile tests and rheology measurement were measured on a dynamic mechanical analyzer (TA, DMA Q800). Dynamic electrical properties were conducted through an electric displacement platform (BOCIC, SC103/10146) and source meter (Keithley, 2400). The contact angles of slurry and electrolyte droplets on the PA separator were measured using an optical contact angle measuring instrument (Dataphysics, OCA15EC).

#### 2.4. Electrochemical measurements

All electrochemical tests used the same electrolyte (2 M ZnSO $_4$ +0.1 M MnSO $_4$ ). The galvanostatic charge/discharge (GCD) performances were carried out on a multi-channel battery test system (LAND, CT2001A) within a potential range of 0.6–1.75V (vs. Zn $^{2+}$ /Zn) at different current rates. Symmetric cells were used to evaluate the electrochemical properties of Zn plating/stripping and the cycling stability. Concretely, the Integrated Separator@Zn symmetric cells were assembled with two same Integrated Separator@Zn electrodes, without additional separator. And the bare Zn symmetric cells were assembled by sandwiching a PA separator between two bare Zn electrodes. The electrochemical impedance spectroscopy (EIS) and cyclic voltammetric (CV) tests were carried on an electrochemical workstation (Zahner, IM6ex). The EIS measurements were performed over a frequency range of 100 kHz to 10 mHz with an applied amplitude of 5 mV. Ionic conductivities were measured by two symmetrical blocking electrodes (stainless steel foil) according to the EIS measurement with an AC amplitude of 5 mV in the frequency ranging from 100 kHz to 10 Hz. The equation of ionic conductivity was calculated by

$$\sigma = \frac{l}{RA}$$

where  $\sigma$  is ionic conductivity, and  $l$ ,  $R$ ,  $A$  represent the thickness, the bulk resistance and the test area, respectively.

### 3. Results and discussion

The fabrication process of an integrated configuration is schematically illustrated in Fig. 1. Initially, pristine Zn foil with a thickness of about 20  $\mu\text{m}$  (Fig. S1a) is used as the anode and the loading template. Then, a certain amount of HCOOH solution containing Zn(TfO) $_2$  and raw

PA is cast onto the Zn foil through a common doctor blading method (named as Zn(TfO) $_2$ -PA protective layer), followed by the rapid attachment of the tailored PA filter membrane onto the surface of undried Zn(TfO) $_2$ -PA protective coating. After that, the obtained sample is promptly transferred to a vacuum oven for drying. In this process, the surface of Zn anode can be precisely polished by the formic acid solution to remove the passivation layer and followed by forming a coherent effective Zn(TfO) $_2$ -PA protective coating integrated with Zn anode. A robust joint between the protective coating and the tailored PA filter membrane can be achieved, which is ascribed to that partial PA layer on the surface of filter membrane can be suitably dissolved by HCOOH and then the derived PA chains can cross-link with the PA chains from the foregoing Zn(TfO) $_2$ -PA protective layer (the separator and protective layer are integrated closely with Zn anode, thus the Zn(TfO) $_2$ -PA//PA is named as Integrated Separator.). Afterwards, the cathode slurry is loaded directly onto another side of PA separator via the blade coating method. In our case,  $\alpha$ -MnO $_2$  NWs, with a diameter of about 50 nm and length of 3–5  $\mu\text{m}$  (Figs. S2 and S3), are used as the cathode active materials to evaluate the effect of the integrated configuration. One-dimensional (1D) nanomaterials are easy to construct interlaced flexible network and the resulting cross-linked structures avail to buffer external stresses [32]. So to ensure the interior electrons transport and flexibility of the cathode component, MWCNTs are chosen to serve as the conductive additive. After the sufficient dispersion and stirring, MnO $_2$  NWs and MWCNTs intertwine and form a conductive network (named as MnO $_2$ -MWCNTs) (Fig. S4). Thus, the whole integrated electrode is free of additional massy non-electrochemical metal current collector. Finally, an all-in-one configuration integrating Zn anode, protective coating, PA separator and cathode into one monolith (Zn//Zn(TfO) $_2$ //PA//PA//MnO $_2$ -MWCNTs) is achieved.

The micro-constructive evolutions during each stage of the preparation process were captured in side- and top-viewed SEM images (Fig. 2). Visibly, the built-in Zn(TfO) $_2$ -PA protective layer is about 30  $\mu\text{m}$  (Fig. 2b). Compared with the smooth surface of the pristine zinc foil (Fig. S1b), the surface of Zn(TfO) $_2$ -PA protective layer becomes rougher (Fig. 2a), which may be due to the re-precipitation of zinc salt and PA chains. The Zn(TfO) $_2$ -PA protective layer is coated onto the Zn anode while glues the PA separator together with Zn anode, forming the so-called Integrated Separator. The Integrated Separator is strongly adhered to the Zn foil and exhibits a flat surface topography (Fig. 2c and d), which is beneficial to the uniformly load of cathode. The side-viewed SEM image (Fig. S5a) further shows that the Integrated Separator and Zn foil are jointed tightly just like being chained together through hinges. The strong adhesion derives from the complex crosslinking role of TfO $^-$ , interaction between Zn $^{2+}$  and the PA chains, as well as the interconnection among PA chains [33,34]. In some detail, Zn $^{2+}$  can interact with amide, forming strong complexes in which the metal atom is coordinately bonded to the carbonyl oxygen atom of the amide group [35].

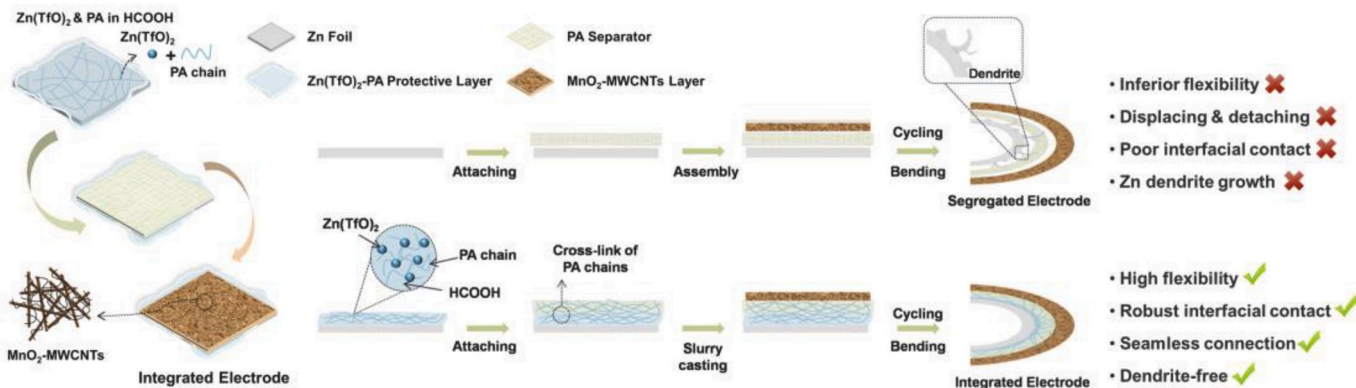


**Fig. 1.** Schematic illustration of the fabrication process of an integrated electrode as well as comparison of sections between the integrated electrode and segregated electrode.

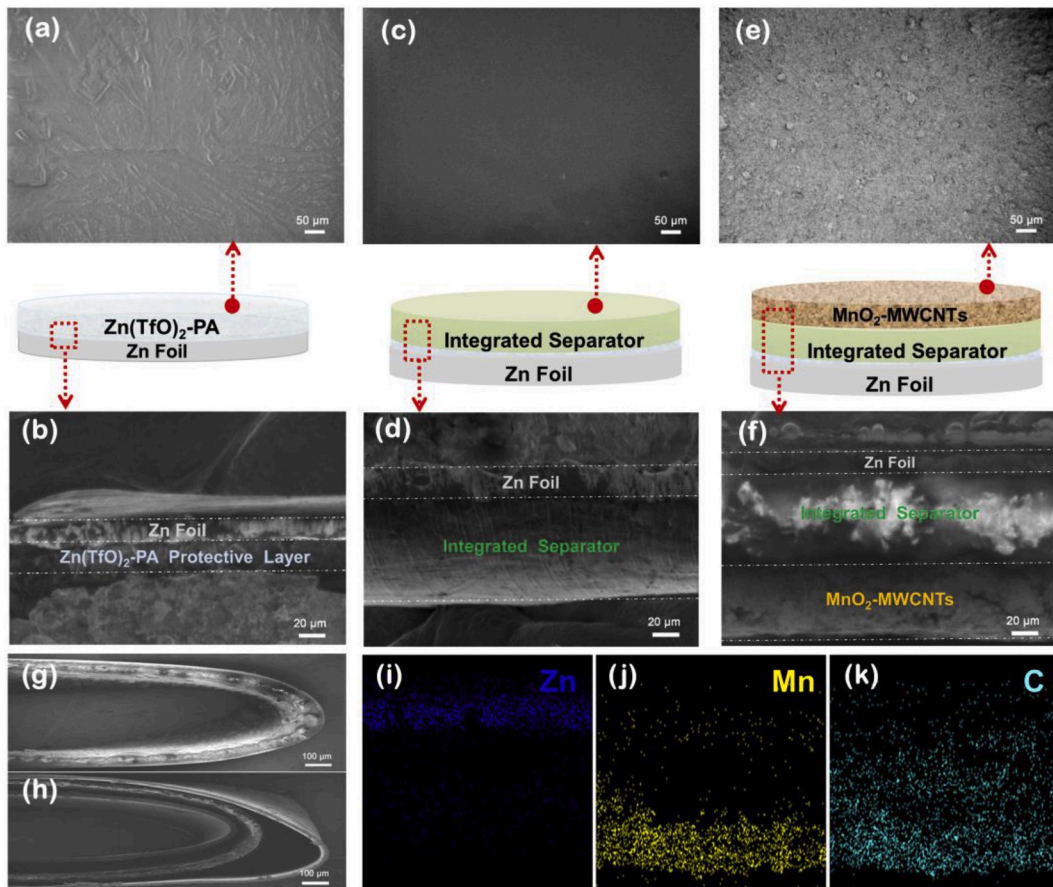


**Fig. 2.** (a,b) Top-viewed and side-viewed SEM images of the  $\text{Zn}(\text{TFO})_2\text{-PA}$  protective layer stabilized Zn foil, respectively. (c,d) Top-viewed (c) and side-viewed (d) SEM images of the Integrated Separator@Zn, respectively. (e,f) Top-viewed (e) and side-viewed (f) SEM images of Integrated Elctetrode, respectively. (g,h) Cross-sectional SEM images of an Integrated Electrode (g) and Segregated Electrode (h) under bending. (i–k) EDS maps of Zn, Mn and C in the cross section of the Integrated Electrode.

$\text{TFO}^-$  anions migrate toward and adhere to the Zn anode, and then some of the adhered  $\text{TFO}^-$  anions cleave the bonding of S=O units [36]. The opened S-O single bond reacts with  $\text{Zn}^{2+}$  in return, forming a strong interaction. Thus, the strong adhesion proceeds between the surface of Zn metal and the protective coating. The forceful interfacial adhesion and intrinsic toughness of the Integrated Separator lay a firm foundation for the flexibility of the integrated configuration. The top-viewed SEM image (Fig. S6) presents that the Integrated Separator can provide a uniform distribution of interpenetrated pores, generally considered to act as an electrolyte reservoir, surrounding the electroactive materials and conducting ions [37]. The measured contact angle at the electrolyte/PA separator interface is  $36.7^\circ$  (Fig. S7a), which directly indicates that the porous structure can facilitate the wetting and preserving of electrolyte. Moreover, Integrated Separator assures the permeability without retarding the ionic conductivity. Through the AC impedance spectra obtained at room temperature (Fig. S8), the ionic conductivity of Integrated Separator is calculated to be  $40.9 \text{ mS cm}^{-1}$ , which extremely approaches to that of common-used filter paper ( $44.4 \text{ mS cm}^{-1}$ ) under the same test condition.

After casting the cathode slurry onto the surface of PA separator and subsequent drying process, the complete Integrated Electrode is obtained. In the ultimate configuration, the side coated with  $\text{MnO}_2\text{-MWCNTs}$  cathode is flat and smooth without any cracks (Fig. 2e). Moreover, neighboring layers are firmly connected with each other. The overall thickness reaches about  $170 \mu\text{m}$  (Fig. 2f), which is consistent with that measured by a micrometer (Fig. S9). Notably, the thickness of the Integrated Electrode is much smaller than that of the conventional separated electrode, which arises from the seamless close contact

between adjacent components and current collector-free in the integrated configuration. Except for a 26.3% reduction in thickness, the weight of Integrated Electrode is also 43.5% less than that of a Segregated Electrode (Fig. S10). Given that the mass of active materials is the same, a thinner electrode thickness will increase the volume energy density of the entire battery, while a lighter weight will increase the mass proportion of active materials and the mass energy density of the entire battery. Then the difference between the seam and seamless constructions is more obvious at bending states. When folded almost to  $180^\circ$ , Integrated Electrode remains an intact seamless structure without relative displacement or detachment between two neighboring components (Fig. 2g). In contrast, Segregated Electrode shows obvious gaps between the neighboring components, which will block the transfer of electrons/ions and increase the polarization of the battery. Cross-sectional EDX mapping of Integrated Electrode demonstrates a well-defined and uniform distribution of Zn, Mn and C (Fig. 2i–k).

In addition, although a blade coating process is carried out to load the cathode during preparation, there is no permeation of coating cathode materials through the separator (Fig. S11), avoiding the inner short circuits. This is ascribed to the network formed from the interconnected  $\text{MnO}_2$  NWs and MWCNTs as well as the micropores ( $0.22 \mu\text{m}$  in pore diameter) of the PA separator. The contact angle of  $\text{MnO}_2\text{-MWCNTs}$  slurry on the surface of PA separator is  $31.1^\circ$  (Fig. S7b), suggesting the favorable wettability and contact between them. Furthermore, to evaluate the binding effect between cathode component and PA separator,  $\text{MnO}_2\text{-MWCNTs}$  slurry coated on pristine PA microfiltration membrane (named as  $\text{MnO}_2\text{-MWCNTs@PA}$ ) was subjected to a repeated bending test. As a result, there is almost no change in the conductivity

after 10000 repeated bending cycles (Fig. S12), and the surface at the bend is flat and smooth without shedding or cracking (Fig. S13a). By contrast, the  $\text{MnO}_2$ -MWCNTs slurry coated on SS foil ( $\text{MnO}_2$ -MWCNTs@SS) suffers from visible cracks on the surface due to the weak adhesion (Fig. S13b). These cracks would cause the desquamations of active materials, capacity loss and increase of contact resistance inside the cathode. Furthermore, the binding stability between cathode component and PA separator in an Integrated Electrode is also superior to that between cathode component and SS current collector in a Segregated Electrode when they are immersed into the electrolyte. As presented in Fig. S14, although both electrodes can keep static stability in the aqueous electrolyte for several days without distinct shedding, Segregated Electrode suffers from much more serious material spalling when exposed to strong external stimulus such as ultrasonication. The above facts indicate that the adhesion between the cathode material and PA separator is significantly stronger than that between the cathode material and SS current collector. This may be ascribed to that, except for the intrinsic intermolecular forces, the binder in the electrode material forms additional strong mechanical interlock with the abundant micropores on the surface of the PA separator for adhesion [38]. While the adhesion between the metal current collector and electrode materials is just dominated by the Van der Waals force. In consequence, based on this elaborate structure, the good flexibility of Integrated Electrode is visually verified. Each component of an Integrated Electrode is firmly

attached without any obvious cracks or material spalling after being bended, twisted or even folded, indicating an excellent mechanical flexibility and robust electrode integrity (Fig. S15).

The same as Li metal anode, where the dendrite-induced inner short circuit is considered to be the dominant mechanism of batteries failure, Zn metal anode also faces with the dead Zn and possible inner short circuit resulting from dendrites [39]. It have been currently proved that a micron-sized interphase, consisted of PA and  $\text{Zn}(\text{TfO})_2$ , plays a significant role to inhibit zinc dendrites and side reactions [29]. Therefore, the Integrated Separator coated on Zn anode with a built-in  $\text{Zn}(\text{TfO})_2$ -PA protective coating is accordingly expected to suppress the Zn dendrites and side reactions substantially. Cycle stability tests of symmetric cells can directly reveal the performance-enhancing effects. As shown in Fig. 3a, with the current density increasing from  $0.1 \text{ mA cm}^{-2}$  to  $2.0 \text{ mA cm}^{-2}$ , the polarization curve of symmetric Integrated Separator@Zn cell keeps steady in each 20 cycles, while the symmetric bare Zn cell occurs irregular voltage curve after the current density rose to  $1.0 \text{ mA cm}^{-2}$ . Then in the long-term plating/stripping cycle test at a typical current density of  $0.2 \text{ mA cm}^{-2}$  (Fig. 3b), a hard short circuit occurred in a very short time (less than 100 h) in the symmetric bare Zn cell. By contrast, the Integrated Separator@Zn symmetric cell evidently prolongs the cycle life, lasting more than 1500 h with a slightly increased overpotential. Note that the polarization voltage of the symmetric Integrated Separator@Zn is invariably smaller than that of the

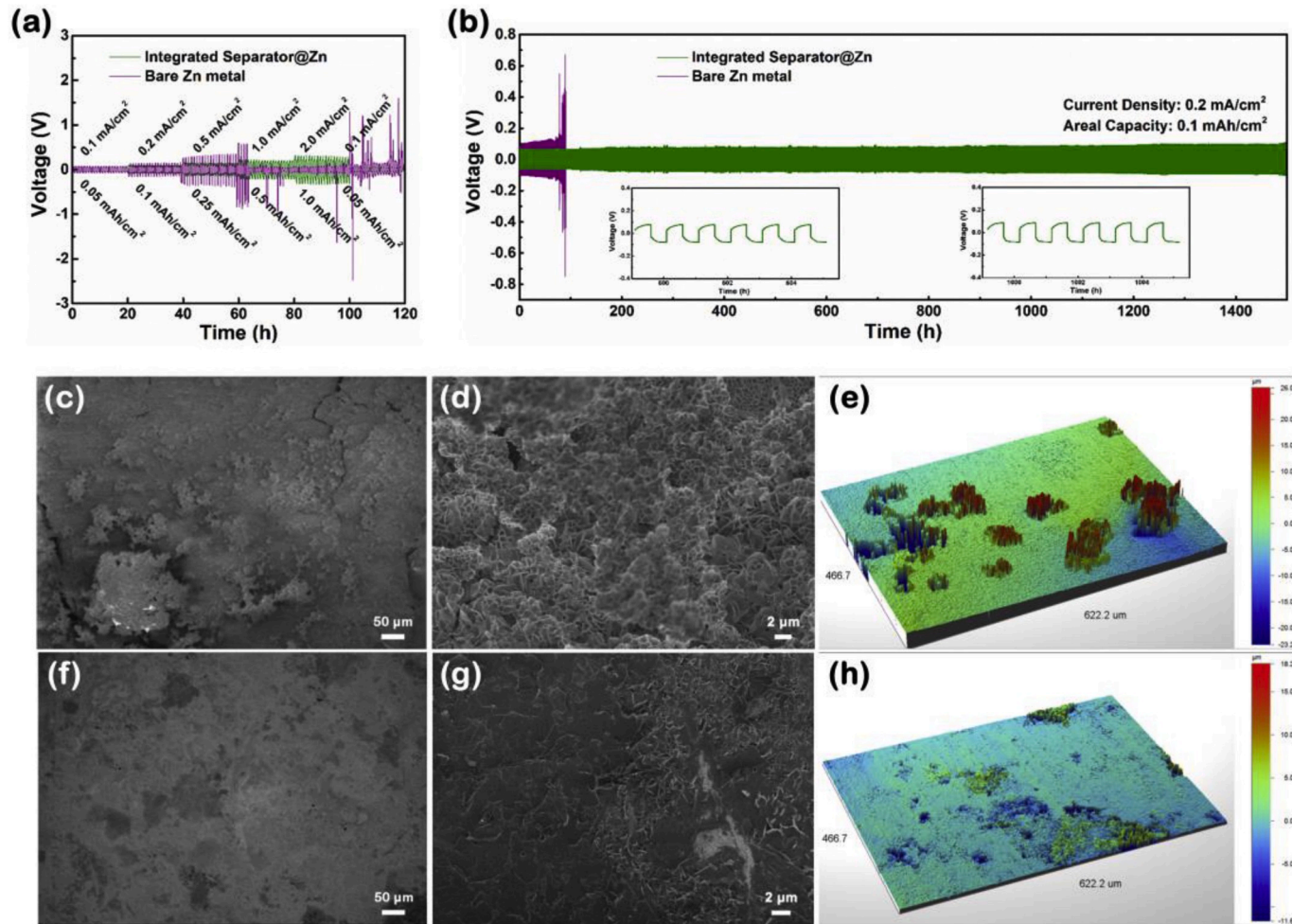


**Fig. 3.** (a) Symmetric cells cycling of the Integrated Separator@Zn and bare Zn electrodes at varied current densities. (b) Long-term galvanostatic cycling of symmetrical Integrated Separator@Zn cell and symmetrical bare Zn cell at a current density of  $0.2 \text{ mA cm}^{-2}$  and an areal capacity of  $0.1 \text{ mAh cm}^{-2}$ . (c–e) Images of SEM and corresponding optical profilometry of bare Zn electrode after 100 cycles at a current density of  $0.2 \text{ mA cm}^{-2}$  in symmetric cell, respectively, observed by top-view; (f–h) Images of SEM and corresponding optical profilometry of the Integrated Separator@Zn electrode after 100 cycles at a current density of  $0.2 \text{ mA cm}^{-2}$  in symmetric cell, respectively, observed by top-view.

symmetric bare Zn cell. These results indicate the protective effect enabled by the built-in  $Zn(TfO)_2$ -PA protective coating in Integrated Separator.

Previous literatures have demonstrated that non-dendritic growth of Zn is desirable for battery cycle performance [25–29]. Thus, we used SEM and 3D surface topograph to examine the morphology of Zn deposition in symmetrical cells to further understand the origins of the improved cyclability (Fig. 3c–h). As observed in the top-viewed SEM images, obvious plaque-shaped dendrites and an uneven surface full of cluster flower-shaped flakes are observed in the bare Zn anode (Fig. 3c and d). Besides, conspicuous cracks appeared on the surface of the bare Zn anode, and the generation of these cracks can be ascribed to the corrosion reaction between electrolyte and zinc anode and large volume change derived from reciprocating Zn stripping and plating. It suggests that unprotected Zn metal can hardly be the anode for flexible aqueous ZIB due to the repeated breakage of fragile. As comparison, the Zn anode stabilized by the built-in protective coating in Integrated Separator has a flat surface morphology without obvious protuberances or cracks (Fig. 3f and g), demonstrating a dendrite-free growth of Zn and the sufficient stability of Integrated Separator to maintain its protective function during cycles. The optical profilometry image depicts that the surface of cycled bare Zn is rather rough (Fig. 3e) with height differences

up to more than 20  $\mu m$ , meanwhile obvious dents derived from corrosion reactions (such as  $H_2$  evolution reaction) appeared on the surface, with a depth differences up to more than 20  $\mu m$ . In contrast, a dendrite-free surface with much smaller height differences and greatly relieved dents directly confirms the inhibition of dendrite growth and side reactions by Integrated Separator (Fig. 3h).

The practical effects of integrated configuration with enhanced interface contact were evaluated by battery tests. To compare the essential electrochemical performances of the integrated ZIB and segregated ZIB, coin-type cells with the same aqueous electrolyte were firstly assembled (the integrated structural batteries are named as Integrated ZIB, and the conventional segregated structural batteries are named as Segregated ZIB). CV is carried out to estimate the ion insertion/extraction behavior of Integrated ZIB, as presented in Fig. 4a. Visually, two well separated reversible redox peaks can be clearly observed, corresponding to a two-step reaction [31]. The two pairs of redox peaks in CV curves are consistent with the two plateaus in the representative GCD profiles of Integrated ZIB at 0.1C shown in Fig. 4b. Specifically, two distinct plateaus located at around 1.4 and 1.3 V in the discharge profiles are attributed to  $Zn^{2+}$ -insertion into  $MnO_2$  NWs, while the plateaus at around 1.53 and 1.58 V in the charge profiles are related to the  $Zn^{2+}$ -extraction from  $MnO_2$ . When cycling these two cells at

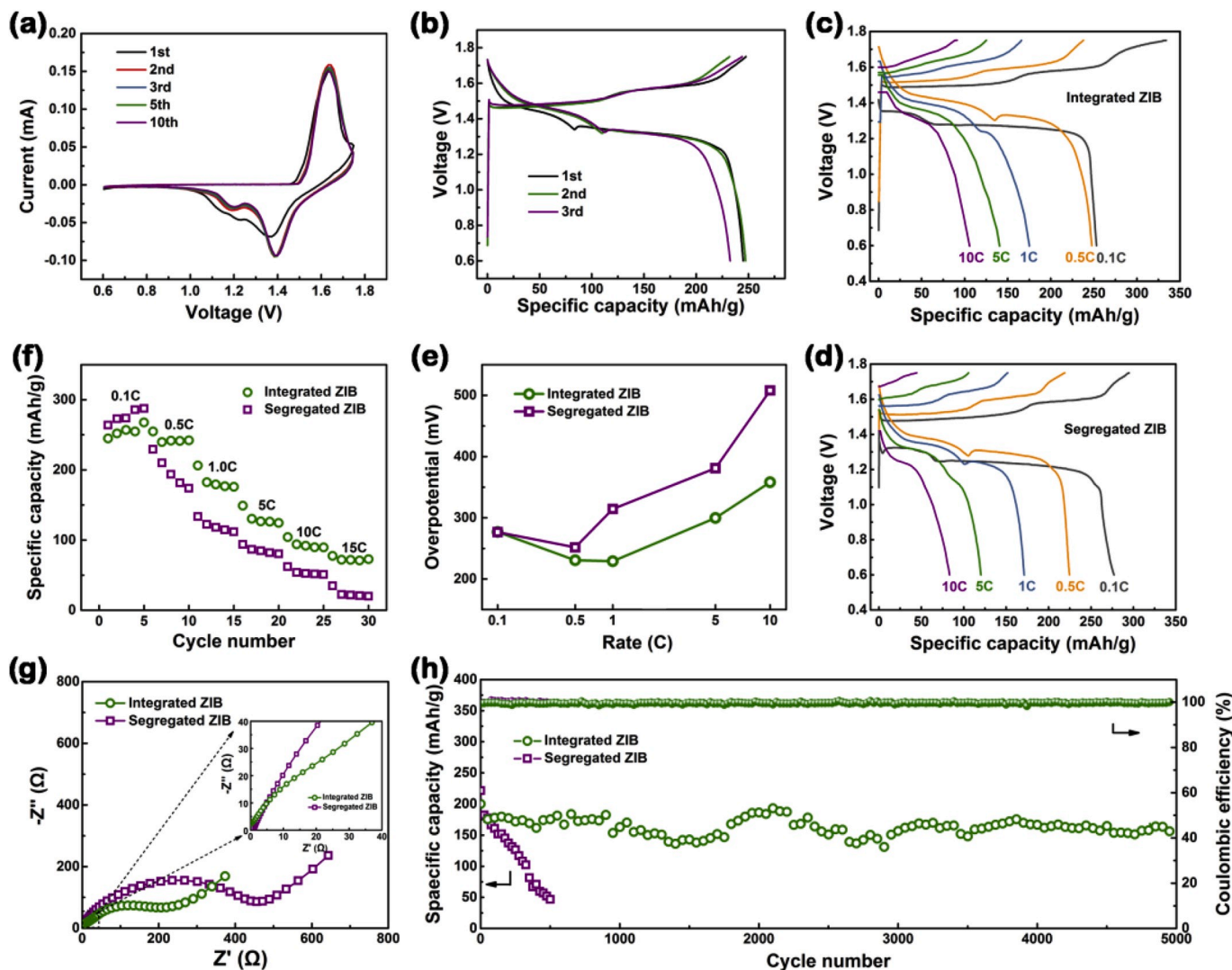


**Fig. 4.** (a) CV curves of an Integrated ZIB at a scan rate of  $0.1 \text{ mV s}^{-1}$ . (b) The first three GCD profiles of an Integrated ZIB at  $0.1\text{C}$  ( $1\text{C} = 308 \text{ mAh g}^{-1}$ , capacity is based on the mass of  $MnO_2$ ). The comparison of electrochemical properties between the Integrated ZIB and Segregated ZIB: (c–d) the GCD profiles at current rates ranging from  $0.1\text{C}$  to  $10\text{C}$ , (e) overpotential-current density plots, (f) rate performances, (g) EIS spectra, (h) long-term cycling performances at  $2\text{C}$ .

current rates of 0.1, 0.5, 1, 5 and 10C for one cycle, Integrated ZIB delivers high specific capacities of 253, 247.6, 175.1, 140.5 and 105.7 mAh g<sup>-1</sup>, respectively (Fig. 4c), evidently higher than that of Segregated ZIB especially when tested at the high rates (Fig. 4d).

Given that Integrated ZIB shows higher capacities at the high rates, we further probed the differences on the reaction kinetics between these two configurations. The discharge plateaus of Segregated ZIB become inclined with higher voltage hysteresis, indicating a slower redox reaction kinetics. The overpotential (the overpotential can be calculated roughly as the voltage difference between charge and discharge at the midpoint of the GCD profiles) at different rates intuitively represents the reaction kinetics in electrochemical process. Note that Integrated ZIB and Segregated ZIB present almost identical overpotentials at the initial low rate (0.1C), while the gaps in overpotentials between these two configurations become larger with the increase of current rates (Fig. 4e). Concretely, the overpotential of Integrated ZIB is 358 mV at 10C. In contrast, a relatively larger overpotential of 508 mV is observed for Segregated ZIB (Table S1). It suggests a kinetically efficient reaction

process for Integrated Electrode with a much smaller barrier since the enhanced contact between neighboring components provides a more continuous electron-/ion-transfer pathway [40]. Consequently, benefiting from the decent smaller polarization and faster electrochemical kinetics, Integrated ZIB exhibits better rate performance as well as lower intrinsic resistance ( $R_s$ ) and charge transfer impedance ( $R_{ct}$ ), as presented in Fig. 4f-g. Integrated ZIB delivers higher discharge capacities of 184, 131, 94 and 73 mAh g<sup>-1</sup> at 1, 5, 10 and 15C, respectively, while Segregated ZIB only shows 120, 85, 54 and 24 mAh g<sup>-1</sup> at the corresponding current rates. Furthermore, after fitting the Nyquist plots by an equivalent circuit model (Fig. S17), Integrated ZIB shows the smaller  $R_s$  and  $R_{ct}$  of 0.2 and 206.4 Ω, much lower than those of Segregated ZIB (with  $R_s$  and  $R_{ct}$  of 1.2 and 441.2 Ω, respectively). To confirm the effect of the protected Zn anode on the actual cycle stability, long-term cycling performance test was conducted (Fig. 4h). Impressively, the reversible capacity of Integrated ZIB remains at 156.4 mAh g<sup>-1</sup> after 5000 cycles at 2C with a capacity retention of 89.4% with the average coulombic efficiency approaching 99.6%. Visibly, the cycle

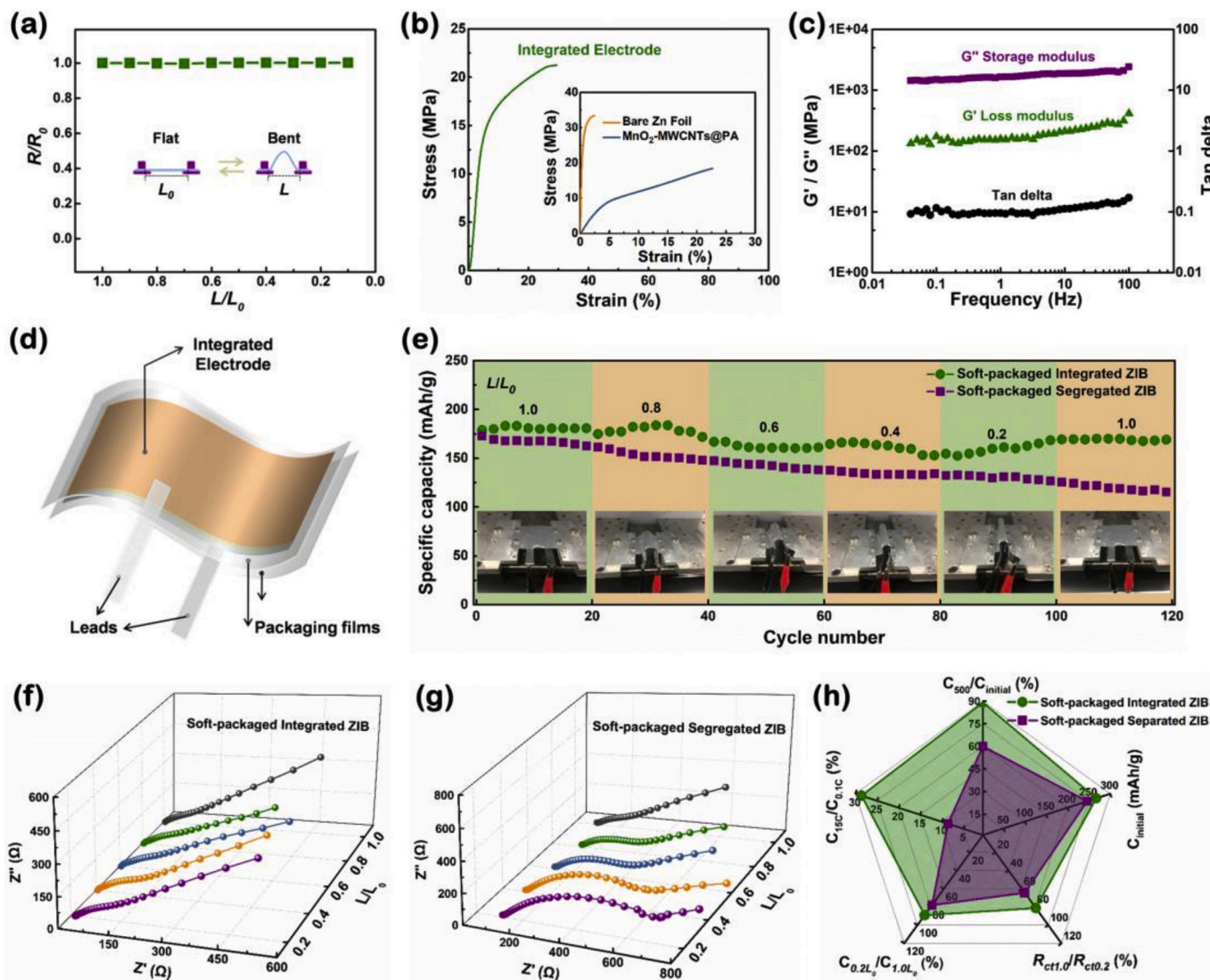


**Fig. 5.** (a) Normalized sheet resistance of the integrated electrode at different bending states, where  $R_0$  and  $L_0$  are the initial resistance and initial length of the electrode, and  $R$  and  $L$  are the resistance and the length between two ends of the electrode under different bending states, respectively. Insets: schematic of flat and bent states. (b) Tensile stress-strain curve of an integrated electrode. Inset: the stress-strain curves of bare Zn foil and  $\text{MnO}_2\text{-MWCNTs@PA}$ . (c) Dynamic thermo-mechanical analysis (DMA) result of an Integrated Electrode showing the viscoelastic properties. (d) Schematic diagram of a Soft-packaged Integrated ZIB. (e) Cycle stability comparison between the Soft-packaged Integrated ZIB and Soft-packaged Segregated ZIB at 2C under different bending states. Insets: optical images of soft-packaged batteries tested under different bending states. (f,g) EIS spectra of the Soft-packaged Integrated ZIBs and Soft-packaged Segregated ZIB under different bending states, respectively. (h) Comparison of the electrochemical performances between the Soft-packaged Integrated ZIB and Soft-packaged Segregated ZIB.

stability of Integrated ZIB is far superior to that of Segregated ZIB, which dramatically drops below to 43 mAh g<sup>-1</sup> after only 500 cycles. As expected, the Zn anode coated with the built-in Zn(TfO)<sub>2</sub>-PA protective layer is observed to be dense and dendrite-free (Fig. S18), which contributes to the boosted durability.

Favorable mechanical flexibility is necessary for flexible energy storage devices, namely, their electrodes can maintain stable properties at different mechanical deformation. Dynamic electrical properties of Integrated Electrode are investigated by measuring the electrical conductivity changes at different bending levels (The degree of bending is controlled by adjusting the distance ( $L$ ) between two ends at which the electrode is fixed, and the initial length is set as  $L_0$ , thus the ratio of  $L/L_0$  represents different bending states). Fig. 5a exhibits the change in electrical conductivity of Integrated Electrode at different bending states. Impressively, Integrated Electrode shows nearly unchanged conductivity even when it is bent to almost folded state. Moreover, due to the robustness of the PA separator, the bending durability of Integrated Electrode has been significantly improved compared with the bare Zn foil. The electrical conductivity of Integrated Electrode remains almost unchanged after more than 2000 bending cycles (Fig. S19a), indicating the structural stability of the whole electrode. Compared with the Integrated Electrode, the bare Zn foil fractures just after 552 bend cycles (Fig. S19b), suggesting that the flexibility and bending resistance of the integrated electrode have been significantly enhanced. This provides an idea for improving the bending performance of rigid metal foils and applying them into the flexible energy storage devices. The mechanical strength of Integrated Electrode is evaluated through the tensile stress-strain curve, as shown in Fig. 5b. Visibly, the integrated structure can withstand a stress higher than 10 MPa with ca. 4% elastic strain, and the Young modulus is more than 250 MPa. The fracture stress and strain of Integrated Electrode are around 21 MPa and 29%, respectively. Consequently, Integrated Electrode can efficiently enhance the load transfer capacity to avoid the relative detachment between the neighboring layers during deformation process. In addition, large volume change derived from reciprocating Zn stripping and plating creates cracks in the Zn anode, inevitably causing drastically deterioration or even invalidation of performances especially at bending strain [41]. Thus, viscoelasticity of Integrated Electrode was measured to examine the balance of mechanical strength and flexibility to accommodate the large volume change in Zn anode. Before the test, Integrated Electrode was immersed in the electrolyte for 7 days to simulate the operating environment in cells. Generally, the storage modulus ( $G''$ ) represents the elastic property while the loss modulus ( $G'$ ) corresponds to the viscous property. As shown in Fig. 5c, the  $G''$  exhibits a modulus above 10<sup>3</sup> Pa, higher than the  $G'$  of 10<sup>2</sup> Pa. And the corresponding Tan delta remains stably at around 10 within the measured frequency range. It indicates that Integrated Separator coated on Zn anode can maintain sufficient viscoelasticity to adapt the mechanical stress produced by volume change while cycling [42]. Based on the above mechanical properties, it is reasonable to conclude that this integrated structure with decent mechanical robustness and flexibility provides a solid foundation for the flexible aqueous ZIBs.

Given the advantageous mechanical flexibility and structural stability of the integrated configuration, these two electrodes with different configurations were encapsulated into Al/plastic soft packages to compare the electrochemical performances (Fig. 5d). The battery fabricated by an Integrated Electrode is named as Soft-packaged Integrated ZIB, while the battery consist of a conventional segregated sandwich structure is named as Soft-packaged Segregated ZIB. Their GCD profiles (Fig. S20) both exhibit two well-defined voltage plateaus, match well with the GCD profiles tested through the coin-cells. But Soft-packaged Integrated ZIB delivers a initial discharge capacity of 267.1 mAh g<sup>-1</sup> at 0.1C, which is higher than that of Soft-packaged Segregated ZIB (246.1 mAh g<sup>-1</sup> at 0.1C). Apart from the gap in the discharge capacity, there are significant differences in the length and height of the voltage plateau. Noteworthily, the difference in overpotential (91 mV)

between the two configurationis already apparent even at a low rate (0.1C), while the difference tested through coin-cells obviously emerges until at 2C. This may be attributed to that the enhanced current density unit area on the surface of electrodes in the soft-packaged batteries would induce a anabatic electrochemical polarization [43]. And also, the intrinsic resistances in soft-packaged batteries are much larger than that in coin-type batteries, leading to more severe ohmic polarization. In contrast, the CV curves of Soft-packaged Integrated ZIB keep the same sharp with those of coin-typed Integrated ZIB and also have a good overlap (Fig. S21). In addition, the cycle stability of Soft-packaged Integrated ZIB is still far superior to that of Soft-packaged Segregated ZIB (Fig. S22). The discharge capacity of Soft-packaged Integrated ZIB stabilizes at 173.7 mAh g<sup>-1</sup> after 500 cycles, which is well consistent with result tested by coin-cell (176.3 mAh g<sup>-1</sup>), indicating a scalable potential of the constructed Integrated Electrode. The impression given is that Soft-packaged Segregated ZIB after 500 cycles is obviously bulging (Fig. S23), which is attributed to the severe H<sub>2</sub> evolution derived from corrosion reactions. However, Soft-packaged Integrated ZIB after cycles is flat without obvious swell. It proves again that the built-in Zn (TfO)<sub>2</sub>-PA protective layer in the integrated configuration has a significant inhibitory effect on the corrosion reactions, boosting the cycle durability.

Except for the electrochemical properties before mechanical deformation, the stable electrochemical performances under different mechanical deformation are crucial criterion to evaluate flexible energy storage devices. The electrochemical stability under different bending states was tested through bending the flexible battery to different levels and then galvanostatically charging and discharging it for 20 cycles under each bending state (inset of Fig. 5e). The representation about the bending level of the flexible battery is consistent with that of the electrode mentioned above. As displayed in Fig. 5e, although the discharge capacity of Soft-packaged Integrated ZIB fluctuates during the cycles, there is no significant capacity decay throughout the test process. As a result, Soft-packaged Integrated ZIB possesses a final discharge capacity of 169 mAh g<sup>-1</sup> after the cycles under different bending states, with a capacity retention of 94.5%. In contrast, the capacity of Soft-packaged Segregated ZIB with conventional stacked configuration was continually degrading, with a much larger capacity drop than that of Soft-packaged Integrated ZIB. Then Soft-packaged Segregated ZIB maintains a final discharge capacity of 114 mAh g<sup>-1</sup> with a capacity retention of 66%, which is lower than the result tested under the flat state (75.8%). Therefore, for Soft-packaged Segregated ZIB, mechanical deformation will further aggravate the poor cycle stability. EIS has been identified as important indicator of electrochemical reaction kinetics. So to further verify the enhancement of interfacial contact especially under different bending states in the integrated configuration, EIS was conducted when flexible battery was under different bending states (Fig. 5f-g). Not surprisingly, the overall impedances of Soft-packaged Integrated ZIB are much lower than those of the conventional Soft-packaged Segregated ZIB. Particularly, Soft-packaged Integrated ZIB exhibits much lower and slightly variable  $R_s$  and  $R_{ct}$  under different bending states (Fig. 5e and Table S2). By contrast, Soft-packaged Segregated ZIB not only displays much larger  $R_s$  and  $R_{ct}$  at initial state, but also exhibits sharp fluctuations in  $R_s$  and  $R_{ct}$  under the maximum bending state.

On the basis of the data presented above, the integrated configuration underpins much more superior electrochemical performances compared with the conventional segregated configuration (Fig. 5h). The improvement of flexible battery performances can be rationalized from the following perspectives: (i) The integrated configuration could efficiently enhance the loadtransfer capacity to avoid the relative detachment between the neighboring layers during deformation process, effectively ensure continuous and stable electron/ion transfer pathway. (ii) Unlike the simple physical contact between stacked components in the segregated configuration, the enhanced interfacial contact between neighboring components significantly lowers the interfacial contact

resistance and decreases the polarization, giving rise to a good rate capability. (iii) The built-in protective layer on the surface of Zn anode can elevate effectively the nucleation barrier and restrict  $Zn^{2+}$  two-dimension diffusion, regulating Zn deposition behavior and suppressing corrosion reaction as well as the Zn dendrites in aqueous environment. In return, this can not only boost the cycle durability, but also avoid the cracks of Zn anode associated with corrosion reaction. (iv) Compared with the weak adhesion between cathode materials and metal current collector, the adhesion between cathode materials and PA separator is greatly enhanced, which can avoid the desquamations of active materials and increase of contact resistance inside the cathode upon bending.

To exemplify the viability for practical applications, Soft-packaged Integrated ZIB was further tested in various situations mimicking real usage. As displayed in Fig. 6a and b, Soft-packaged Integrated ZIB can hold the discharge profile without distinct deterioration and keep the CV curves with an excellent overlap when folded nearly to 180° ( $L/L_0 = 0.2$ ), suggesting that even almost the maximum bending degree has negligible effect on the electrochemical behavior of Soft-packaged Integrated ZIB. Repeated bending trial was also carried out on Soft-

packaged Integrated ZIB. Shown in Fig. 6c is that more than 90% of capacity is retained after 1000 bending cycles. Such desirable mechanical flexibility and electrochemical stability endow the Soft-packaged Integrated ZIB with great feasibility in the application in wearable and portable electronics. Besides, in practical applied environment, batteries need to be integrated in series or parallel to enlarge the output voltage or current, which enables them to meet high energy and power needs. As presented in Fig. 6d, compared to a single Soft-packaged Integrated ZIB with an operating voltage of 1.75 V, two batteries connected in series can achieve a double output voltage (i.e., 3.5 V) with an analogous discharge time. And after connecting two batteries in parallel, the overall discharge time is nearly twofold that of a single battery. To intuitively demonstrate the excellent flexibility and application potential of Soft-packaged Integrated ZIB, two batteries were assembled in series and pasted together with an electroluminescent belt (Fig. 6f). Impressively, the electroluminescent belt could be lit well without perceptible changes in brightness when the assembly was under different bending states (Fig. 6g). Moreover, the voltages of open circuit (VOCs) of Soft-packaged Integrated ZIB hold constant as the bending degree changed. The above features fully indicate that the Soft-packaged

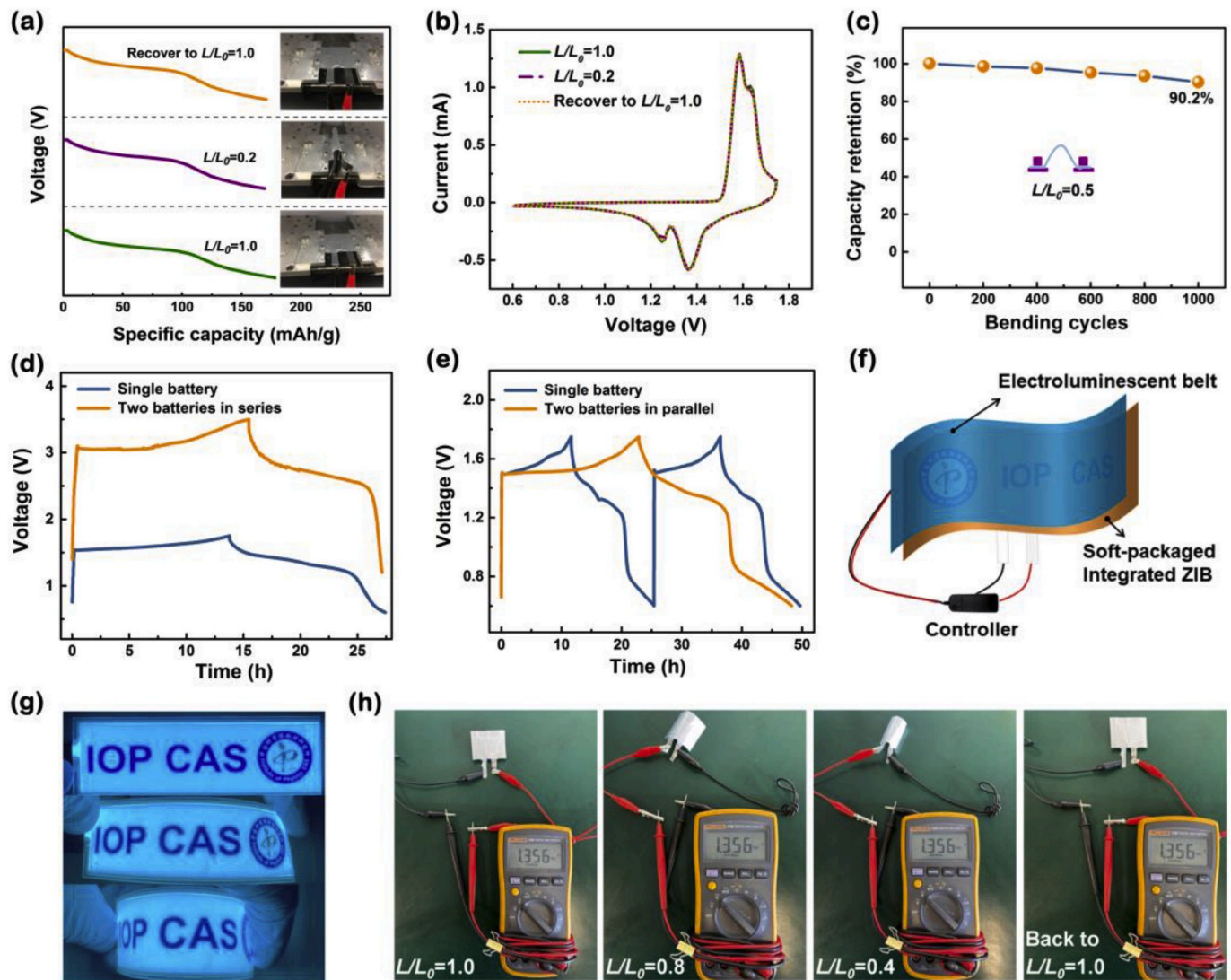


**Fig. 6.** (a) Galvanostatic discharge curves under bending states for a Soft-packaged Integrated ZIB. (b) The CV curves of a Soft-packaged Integrated ZIB under different bending states with excellent overlap. (c) Dependence of capacity retention for a Soft-packaged Integrated ZIB on bending cycles. (d) GCD profiles of two Soft-packaged Integrated ZIBs connected in series. (e) GCD profiles of two Soft-packaged Integrated ZIBs connected in parallel. (f) Schematic diagram of a flexible display unit using a flexible electroluminescent belt powered by Soft-packaged Integrated ZIBs. (g) The optical images of the flexible electroluminescent belt (size 30 × 80 mm) lit by Soft-packaged Integrated ZIBs under different bending states. (h) The VOCs of a Soft-packaged Integrated ZIB under different bending states.

Integrated ZIB can serve as a viable and reliable power supply for practical applications in flexible and portable electronic fields.

#### 4. Conclusions

In summary, we have demonstrated an elaborate strategy to engineer an integrated configuration for ZIBs with robust mechanical flexibility. Compared with the conventional segregated battery structure, the as-designed integrated configuration greatly improves the flexibility and electrochemical performances of ZIBs mainly in four ways: (1) continuous seamless connection prevents the relative displacement or detachment between the neighboring components at different mechanical deformations to ensure the steady load- and/or electron-transfer; (2) the enhanced interfacial contact between neighboring components significantly lowers the interfacial contact resistance and decreases the polarization; (3) the built-in Zn anode protective coating suppresses the dendrite growth, regulates Zn deposition behavior and reduces parasitic reactions between Zn and electrolyte; (4) the robust adhesion between cathode materials and PA separator avoids the desquamations of active materials and increase of contact resistance inside the cathode upon bending. Above features not only enable desirable flexibility and structural stability but endow superior electrochemical kinetics and stable electrochemical performances under different bending states for ZIB. Additionally, the integrated configuration brings the feasibility of cathode part itself replacing the metal current collector and achieves the lightening and thinning of battery. Meanwhile, the preparation method is manageable and scaleable as well as compatible with current battery manufacturing processes, which means potentially cost-effective. Therefore, the proposed integrated configuration represents a promising route to realize practical ZIB with long life and high flexibility.

#### Declaration of competing interest

The authors declare that they have no known competing financial interests or personal relationships that could have appeared to influence the work reported in this paper.

#### CRediT authorship contribution statement

**Penghui Chen:** Conceptualization, Methodology, Validation, Investigation, Data curation, Writing - original draft. **Weiya Zhou:** Conceptualization, Resources, Writing - review & editing, Supervision. **Zhuojian Xiao:** Formal analysis. **Shaoqing Li:** Validation, Formal analysis. **Zibo Wang:** Formal analysis. **Yanchun Wang:** Resources, Data curation. **Sishen Xie:** Conceptualization, Supervision.

#### Acknowledgements

This work was supported by the National Key R&D Program of China (Grant No. 2018YFA0208402), the National Natural Science Foundation of China (11634014, 51172271 and 51372269), the “Strategic Priority Research Program” of the Chinese Academy of Sciences (XDA09040202).

#### Appendix A. Supplementary data

Supplementary data to this article can be found online at <https://doi.org/10.1016/j.nanoen.2020.104905>.

#### References

- [1] M. Armand, J.M. Tarascon, *Nature* 451 (2008) 652–657.
- [2] L. Wang, X.M. Fu, J.Q. He, X. Shi, T.Q. Chen, P.N. Chen, B.J. Wang, H.S. Peng, *Adv. Mater.* 31 (2019), 190197.
- [3] Z.X. Liu, F.N. Mo, H.F. Li, M.S. Zhu, Z.F. Wang, G.J. Liang, C.Y. Zhi, *Small Methods* 2 (2018), 1800124.
- [4] X.L. Yu, J.J. Deng, X.Y. Yang, J. Li, Z.H. Huang, B.H. Li, F.Y. Kang, *Nano Energy* 67 (2020), 104256.
- [5] A. Sumboja, J. Liu, W.G. Zheng, Y. Zong, H. Zhang, Z. Liu, *Chem. Soc. Rev.* 47 (2018) 5919–5945.
- [6] H.F. Li, L.T. Ma, C.P. Han, Z.F. Wang, Z.X. Liu, Z.J. Tang, C.Y. Zhi, *Nano Energy* 62 (2019) 550–587.
- [7] M.Q. Liu, Q.H. Zhao, H. Liu, J.L. Yang, X. Chen, L.Y. Yang, Y.H. Cui, W.Y. Huang, W.G. Zhao, A.Y. Song, Y.T. Wang, S.X. Ding, Y.L. Song, G.Y. Qian, H.B. Chen, F. Pan, *Nano Energy* 64 (2019), 103942.
- [8] A. Konarov, N. Voronina, J.H. Jo, Z. Bakenov, Y.K. Sun, S.T. Myung, *ACS Energy Lett.* 3 (2018) 2620–2640.
- [9] C.X. Zu, H. Li, *Energy Environ. Sci.* 4 (2011) 2614–2624.
- [10] H.J. Peng, J.Q. Huang, X.B. Cheng, Q. Zhang, *Adv. Energy Mater.* 7 (2017), 1700260.
- [11] J. Zhao, H. Ren, Q.H. Li, D. Yuan, S.B. Xi, C. Wu, W.M. Jr., J.M. Ma, W. Fang, Y. Zheng, C.F. Du, M. Srinivasan, Q.Y. Yan, *Nano Energy* 62 (2019) 94–102.
- [12] W. Zhang, P. Feng, J. Chen, Z.M. Sun, B.X. Zhao, *Prog. Polym. Sci.* 88 (2019) 220.
- [13] Z. Wang, J. Hu, L. Han, Z. Wang, H. Wang, Q. Zhao, J. Liu, F. Pan, *Nano Energy* 56 (2019) 92–99.
- [14] L. Xu, S. Tang, Y. Cheng, K.Y. Wang, J.Y. Liang, C. Liu, Y.C. Cao, F. Wei, L.Q. Mai, *Joule* 2 (2018) 1991–2015.
- [15] H.C. Gao, S. Xin, L.G. Xue, J.B. Goodenough, *Inside Chem.* 4 (2018) 833–844.
- [16] B.Y. Tang, L.T. Shan, S.Q. Liang, J. Zhou, *Energy Environ. Sci.* 12 (2019) 3288–3304.
- [17] G. Zhou, F. Li, H.M. Cheng, *Energy Environ. Sci.* 7 (2014) 1307–1338.
- [18] Z.P. Wang, J.L. Cheng, Q. Guan, H. Huang, Y.C. Li, J.W. Zhou, W. Ni, B. Wang, S. He, H.S. Peng, *Nano Energy* 45 (2018) 210–219.
- [19] Z.Q. Niu, H.B. Dong, B.W. Zhu, J.Z. Li, H.H. Hng, W.Y. Zhou, X.D. Chen, S.S. Xie, *Adv. Mater.* 25 (2013) 1058–1064.
- [20] P.S. Luan, N. Zhang, W.Y. Zhou, Z.Q. Niu, Q. Zhang, L. Cai, X. Zhang, F. Yang, Q. X. Fan, W.B. Zhou, Z.J. Xiao, X.G. Gu, H.L. Chen, K.W. Li, S.Q. Xiao, Y.C. Wang, H. P. Liu, S.S. Xie, *Adv. Funct. Mater.* 26 (2016) 8178–8184.
- [21] C.L. Jiang, Y. Fang, J.H. Lang, Y.B. Tang, *Adv. Energy Mater.* 7 (2017), 1700913.
- [22] G.M. Zhou, L. Li, D.W. Wang, X.Y. Shan, S.F. Pei, F. Li, H.M. Cheng, *Adv. Mater.* 27 (2015) 641–647.
- [23] M.J. Yao, R. Wang, Z.F. Zhao, Y. Liu, Z.Q. Niu, J. Chen, *ACS Nano* 12 (2018) 12503–12511.
- [24] S.M. Xu, D.W. McOwen, L. Zhang, G.T. Hitz, C.W. Wang, Z.H. Ma, C.J. Chen, W. Luo, J.Q. Dai, Y.D. Kuang, E.M. Hitz, K. Fu, Y.H. Gong, E.D. Wachsman, L.B. Hu, *Energy Storage Mater* 15 (2018) 458–464.
- [25] J.W. Zhao, J. Zhang, W.H. Yang, B.B. Chen, Z.M. Zhao, H.Y. Qiu, S.M. Dong, X. H. Zhou, G.L. Cui, L.Q. Chen, *Nano Energy* 57 (2019) 625–634.
- [26] J. Yi, P.C. Liang, X.Y. Liu, K. Wu, Y.Y. Liu, Y.G. Wang, Y.Y. Xia, J.J. Zhang, *Energy Environ. Sci.* 11 (2018) 3075–3095.
- [27] Q. Yang, G.J. Liang, Y. Guo, Z.X. Liu, B.X. Yan, D.H. Wang, Z.D. Huang, X.L. Li, J. Fan, C.Y. Zhi, *Adv. Mater.* 31 (2019), 1903778.
- [28] L.T. Kang, M.W. Cui, F.Y. Jiang, Y.F. Gao, H.J. Luo, J.J. Liu, W. Liang, C.Y. Zhi, *Adv. Energy Mater.* 8 (2018), 1801090.
- [29] Z.M. Zhao, J.W. Zhao, Z.L. Hu, J.D. Li, J.J. Li, Y.J. Zhang, C. Wang, G.L. Cui, *Energy Environ. Sci.* 12 (2019) 1938–1949.
- [30] K. Wang, S. Luo, Y. Wu, X.F. He, F. Zhao, J.P. Wang, K.L. Jiang, S.S. Fan, *Adv. Funct. Mater.* 23 (2013) 846–853.
- [31] B.K. Wu, G.B. Zhang, M.Y. Yan, T.F. Xiong, P. He, L. He, X. Xu, L.Q. Mai, *Small* 14 (2018), 1703850.
- [32] L.Q. Mai, J.Z. Sheng, L. Xu, S.S. Tan, J.S. Meng, *Acc. Chem. Res.* 51 (2018) 950–959.
- [33] J.F. Snyder, R.H. Carter, E.D. Wetzel, *Chem. Mater.* 19 (2007) 3793–3801.
- [34] S. Zahurak, M. Kaplan, E. Rietman, D. Murphy, R. Cava, *Macromolecules* 21 (1988) 654–660.
- [35] Y. Feng, A. Schmidt, R.A. Weiss, *Macromolecules* 29 (1996) 3909–3917.
- [36] T. Shiga, Y. Kato, M. Inoue, N. Takahashi, Y. Hase, *J. Phys. Chem. C* 119 (2015) 3488–3494.
- [37] W.B. Kong, L.J. Yan, Y.F. Luo, D.T. Wang, K.L. Jiang, Q.Q. Li, S.S. Fan, J.P. Wang, *Adv. Funct. Mater.* 27 (2017), 1606663.
- [38] W.S. Kim, H. Yun, J.J. Lee, H.T. Jung, *Int. J. Adhesion Adhes.* 30 (2010) 408–417.
- [39] F. Wang, O. Borodin, T. Gao, X. Fan, W. Sun, F. Han, A. Faraone, J.A. Dura, K. Xu, C. Wang, *Nat. Mater.* 17 (2018) 543–549.
- [40] X.Z. Chen, W.J. He, L.X. Ding, S.Q. Wang, H.H. Wang, *Energy Environ. Sci.* 12 (2019) 938–944.
- [41] Z.A. Yu, D.G. Mackanic, W. Michaels, M. Lee, A. Pei, D.W. Feng, Q.H. Zhang, Y. C. Tsao, C.V. Amanchukwu, Y. Cui, Z.N. Bao, *Joule* 3 (2019) 1–16.
- [42] C.D. Han, M.S. Jhon, *J. Appl. Polym. Sci.* 32 (1986) 3809–3840.
- [43] X.B. Cheng, C. Yan, J.Q. Huang, P. Li, L. Zhu, L. Zhao, Y. Zhang, W. Zhu, S.T. Yang, Q. Zhang, *Energy Storage Mater* 6 (2017) 18–25.



**Penghui Chen** received his Master degree from Sichuan University in 2016. He is currently a Ph.D. candidate in the Institute of Physics, Chinese Academy of Sciences. His research interests mainly focus on the synthesis and characterization of nanomaterials as well as their applications in electrochemical energy storage devices.



**Zibo Wang** received his B.S. degree from Beijing University of Technology in 2017. He is currently a Ph.D. candidate in the Institute of Physics, Chinese Academy of Sciences. He has been working on the growth, characterization and application of carbon nanomaterials.



**Weiya Zhou** is a professor of Condensed Matter Physics at the Institute of Physics, Chinese Academy of Sciences (CAS). She received her Ph.D. degree from Jilin University in 1990. After a postdoctoral research at the University of Groningen, the Netherlands, she joined the Institute of Physics, CAS. She has been engaged a long time in the investigation of carbon nanotubes, graphene or the relevant nanomaterials and their characterization as well as their physical properties and possible applications.



**Yanchun Wang** is a senior engineer at the Institute of Physics, Chinese Academy of Sciences (CAS). He received his Ph.D. degree from the Institute of Physics, CAS in 2008. After a postdoctoral research at Hongkong University from 2009 to 2011, he joined the Institute of Physics at CAS. He has been working on the characterization and application of carbon nanomaterials.



**Zhuojian Xiao** received his B.S. degree in material physics from the University of Science and Technology, Beijing in 2012. He gained his Master degree (2015) and Ph.D. degree (2019) from the Institute of Physics, Chinese Academy of Sciences. His research interests mainly focus on synthesis and application of nanomaterials based on graphene.



**Sishen Xie** is a physicist and an academician at the Chinese Academy of Sciences (CAS) and a fellow of the Third World Academy of Sciences. He graduated in physics from Peking University in 1965 and received his Ph.D. degree in 1983 from the Institute of Physics at CAS. Since 1994, he has been a professor of Condensed Matter Physics at the Institute of Physics, CAS. His research interests are mainly in solid-state and materials physics, including high-T<sub>c</sub> superconductivity of oxides, phase diagrams and relations of inorganic systems, fullerenes, and nanomaterials.



**Shaoqing Li** received his Master's degree from Beijing Institute of Nanoenergy and Nanosystems (BINN), Chinese Academy of Sciences (CAS) in 2018. He is currently a Ph.D. candidate in Condensed Matter Physics at the Institute of Physics, Chinese Academy of Sciences. His current research interests focus on flexible rechargeable batteries and novel non-volatile memory devices.